ACTA PHYSICA POLONICA A No. 1 Vol. **149** (2026)

Study of the Combination of Nano and Femto Second Laser Pulses to Generate Gold Plasma for Water Window Emission

Z.A. Alyahya* and W.H. Mahdi

Department of Physics, College of Education for Women, University of Kufa, Najaf 54003, Iraq

Received: 20.08.2025 & Accepted: 17.12.2025

Doi: 10.12693/APhysPolA.149.46

*e-mail: zahraaa.alyahya@student.uokufa.edu.iq

In this study, we employed the one-dimensional hydrodynamic simulation code MED103 to theoretically investigate the generation and spatial–temporal evolution of highly charged gold ions induced by a double-pulse Ti:sapphire laser system. A pre-pulse of 10 ns duration and intensity of 8.5×10^{11} W/cm^2 and a main pulse of 100 fs duration and intensity of 7×10^{16} W/cm^2 were used to irradiate a 20 μm thick gold target. The temporal separation between the pulses was varied from 0 to 10 ns to explore its effect on the formation of ion charge states ranging from Au^{19+} to Au^{34+}, with particular emphasis on optimizing conditions for soft X-ray emission within the water window spectral range. Simulation results reveal that the most favorable ion fractions for ion stages (Au^{25+}–Au^{30+}), which are key contributors to unresolved transition arrays in the water window region, are predominantly formed at delay times between 5.8 and 7.5 ns. Additionally, both the electron temperature and average charge state were found to decrease with increasing delay time, affecting the ion distribution and emission characteristics. These results highlight the importance of precise delay time control in tailoring plasma conditions for efficient soft X-ray generation in high-Z laser-produced plasmas.

topics: high-Z plasma, highly charged ion, gold plasma, soft X-rays

1. Introduction

Laser-produced plasma (LPP) is considered a powerful and promising source for soft X-rays (SXR) [1, 2]. High-Z plasma can generate highly charged ions (HCI) that emit intense, short-pulsed soft X-rays in a spectral region referred to as the water window (WW), extending from the absorption edge of oxygen to the absorption edge of carbon, at wavelengths between 2.3 and 4.4 nm, where water exhibits transparency to X-rays [3]. The importance of SXR emission in the WW region is highlighted in biological research [4], especially for the advancement of soft X-ray microscopy [5], contact microscopy [6], and correlative fluorescence and soft X-ray (FLM-SXR) microscopy [7], which enable imaging of cells and live aquatic biological specimens with high spatial resolution and high contrast [8, 9]. While synchrotron sources, free-electron lasers [10], and tabletop laser sources [11] can provide intense soft X-rays, their high cost and limited access make them impractical. As an alternative, LPP sources enable the generation of intense, broadband SXR emissions through a high-power laser interaction with the target [12]. High-Z elements like gold ($Z = 79$) are particularly effective targets due to their ability to produce unresolved transition arrays (UTAs) resulting from the $4d$–$4f$ and $4f$–$5g$ electronic transitions between energy states in the form of intense quasi-continuous radiation, mainly due to $n = 4 - n = 4$ ($\Delta n = 0$) and $n = 4 - n = 5$ ($\Delta n = 1$) transitions in HCI ions [13]. Previous studies have focused on various methods to enhance SXR emission from gold plasmas, including the use of foam, foil, or multilayer targets, primarily under single-pulse laser irradiation [14–18]. However, the use of double-pulse laser techniques has demonstrated greater control over plasma conditions by allowing fine-tuning of the pre-plasma environment before the arrival of the main pulse [19, 20]. Despite this, detailed investigations into how the inter-pulse delay affects the formation and evolution of highly charged ions, particularly those relevant to WW emissions, remain limited.

In this work, we employ the one-dimensional Lagrangian hydrodynamic code MED103 to simulate the interaction of a double-pulse Ti:sapphire laser with a cylindrical gold target of 20 μm radius. We systematically investigate how varying the time delay between the pre-pulse and the main pulse (both at the 800 nm wavelength of the Ti:sapphire laser) affects the spatial and temporal evolution of gold ion charge states from Au^{19+} to Au^{34+}, with a particular focus on ions (Au^{20+}, Au^{25+}, Au^{26+}, and Au^{30+}). Our results highlight an optimal delay time range that enhances the generation of mid- to high-charge states (Au^{25+}–Au^{30+}), thus suggesting practical strategies for improving the efficiency of SXR sources.

2. Computational methods

To simulate the spatial-temporal evolution of the distribution of ion concentration in gold plasma, we used the 1D-Lagrangian hydrodynamic code MED103 (an upgraded version of Medusa). The code assumes the plasma is a neutral mixture and describes it using 4 main dependent variables, which represent the velocity u, density ρ, ion temperature T_i, and electron temperature T_e as functions of time and space. The code applies a two-fluid model, where electrons are treated as one subsystem and ions as the second subsystem. Each subsystem has a specific heat temperature, internal energy U, pressure p, and so on, while both share a hydrodynamic velocity, the value of which is the same for the two subsystems. The Navier–Stokes equation describes the plasma motion via a moving Lagrangian mesh divided into 400 independent cells within a cylindrical geometry target. Each cell is guided by the primary dependent variables. It is presumed that ions behave as non-degenerate perfect gases, whereas electrons behave as perfect gases that may be either non-degenerate, partially degenerate, or wholly degenerate [21]. The system is described starting from the equations of motion

$$\rho \frac{\mathrm{d}u}{\mathrm{d}t} = -\nabla p, \tag{1}$$

where u is the velocity of the plasma and p is the hydrodynamic pressure. The energy equation for each subsystem is

$$C_V \frac{\mathrm{d}T}{\mathrm{d}t} + B_T \frac{\mathrm{d}\rho}{\mathrm{d}t} + p\frac{\mathrm{d}V}{\mathrm{d}t} = S, \tag{2}$$

where S [W/kg] is the power per unit mass. Here, the internal energy of the system is $C_V = (\frac{\partial U}{\partial T})_\rho$, and $B_T = (\frac{\partial U}{\partial \rho})_T$. The relation between the electron and ion densities is

$$n_e = Z\, n_i, \tag{3}$$

and n_e is given in m^{-3}. The average charge Z was calculated as $Z = \sum_k f_k Z_k$. Here, f_k is the fraction of ions of species k ($\sum_k f_k = 1$), and Z_k is the charge number of individual ion species. The number density of ion species n_k is described by $n_k = f_k n_i$.

In MED103 code, laser energy deposition is implemented primarily through inverse Bremsstrahlung absorption, with high-field corrections included to account for strong laser intensities [22]. The absorbed energy is coupled to the free-electron energy balance equation, allowing subsequent energy transfer to ions via electron–ion collisions. This treatment provides a realistic description of laser heating in dense plasmas, as detailed in [21]. The code incorporates the equation of motion and equations of state for the plasma, as well as atomic processes (excitation, ionization, and recombination). MED103 employs a time-dependent average atom model, solving the energy equation implicitly and the equation of motion explicitly. Users can control various target and laser parameters, including the number of pulses, wavelength, pulse width and intensity, and inter-pulse delay [22]. The code has been extensively tested and applied in various works [23–25].

3. Results and discussion

Hydrodynamic simulations were performed using a double-pulse laser configuration to generate gold plasma. The pre-pulse had a 10 ns duration, an intensity of 8.5×10^{11} W/cm^2, and a laser spot diameter of 25 μm, while the main pulse was 100 fs long, with a higher intensity of 7×10^{16} W/cm^2, and a laser spot diameter of 20 μm. Both pulses originated from an 800 nm Ti:sapphire laser system, with a variable peak-to-peak time separation in the range between 0 and 10 ns. The focus of this study was to investigate the effect of pulse delay on the generation and evolution of highly charged gold ions (Au^{19+} to Au^{34+}) that are responsible for emitting radiations in the water window soft X-ray region. Four representative charge states (Au^{20+}, Au^{25+}, Au^{26+}, and Au^{30+}) were selected for detailed analysis at four delay times (1.5, 5.8, 7.5, and 9.8 ns).

Figure 1 shows the spatial–temporal profiles of the electron temperature (T_e) and average charge state (Z_{ave}) of the plasma for four selected delay times: 1.5, 5.8, 7.5, and 9.8 ns. As seen in Fig. 1a–d, increasing the delay time between the laser pulses leads to a noticeable reduction in the peak electron temperature. This trend can be attributed to the fact that, at short delay times, the peaks of two laser pulses were too close to each other. So, the main pulse reheated electrons to a higher temperature. In addition, the high-intensity main pulse interacts with a denser and less expanded preformed plasma creating compressed plasma, where the high electron density enhances collisional absorption, and the existing ionization level facilitates efficient energy coupling, resulting in a sharp rise in the T_e value. The existing ions absorb more energy, generating higher ion species. In contrast, longer delay times allow the pre-plasma to expand and cool, reducing density and weakening absorption mechanisms, which in turn reduces the peak T_e. Similarly, Fig. 1e–h shows that the average charge state, evaluated immediately after the main

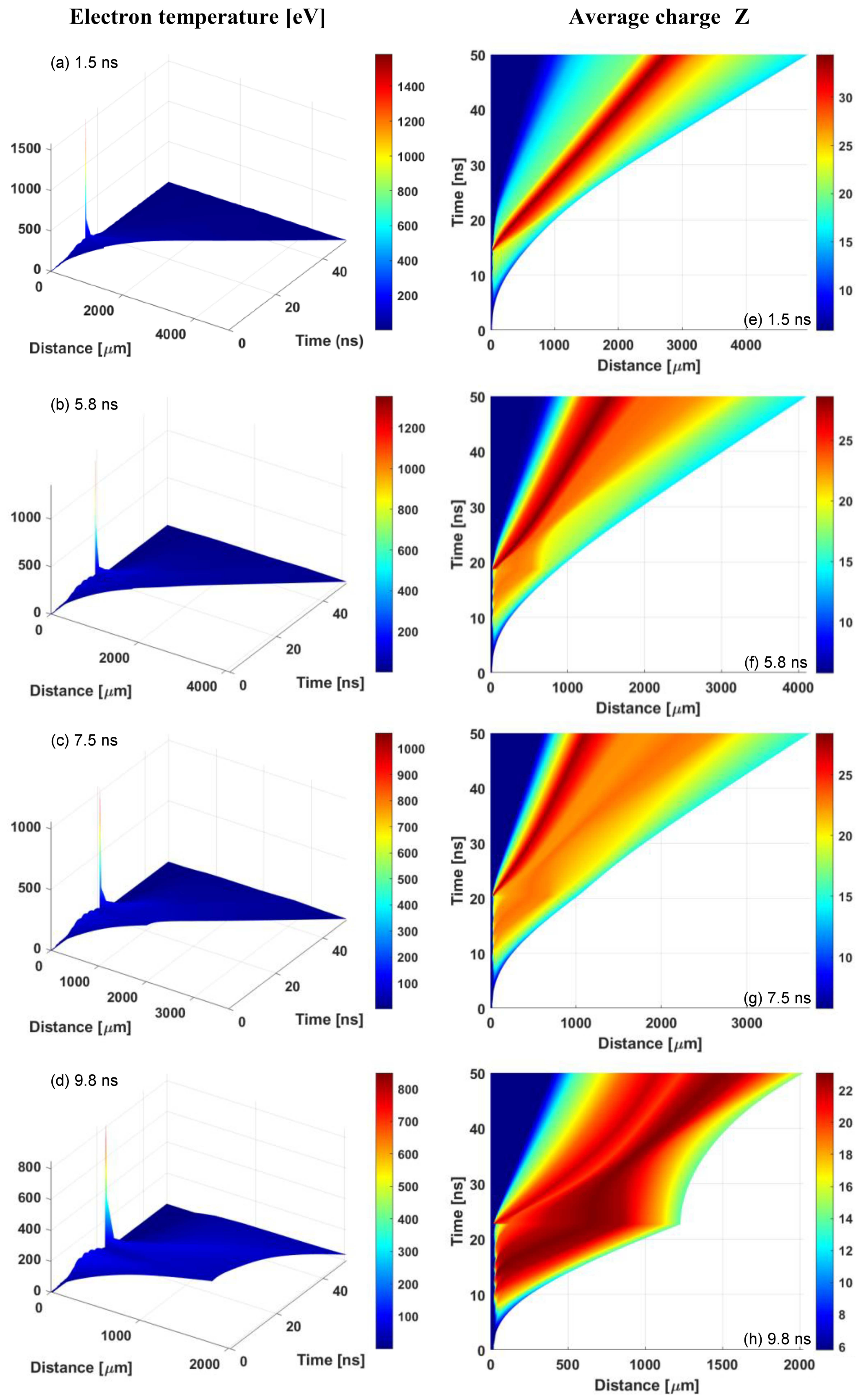

Fig. 1. Spatial–temporal hydrodynamic maps of a gold target that was irradiated with two pulses with four separation times. Panels show profiles of (a–d) electron temperature and (e–h) average charge at delay times of 1.5, 5.8, 7.5, and 9.8 ns.

TABLE I

Effects of pulse separation time on gold plasma parameters and ion distribution.

Delay time [ns]	$T_{e\,\max}$ [eV]	$Z_{ave\,\max}$	Maximum ion fraction	Dominant ions
1.5	1584	34.4	0.40	Au^{19+}–Au^{22+}
5.8	1356	28	0.30	Au^{22+}–Au^{26+}
7.5	1060	28	0.30	Au^{22+}–Au^{26+}
9.8	849	23	0.70	Au^{20+}

pulse, decreases with increasing pulse separation time, consistent with the corresponding reduction in electron temperature, highlighting the sensitivity of ionization levels to T_e under the present irradiation conditions. It should be emphasized that this trend is specific to the input laser parameters assumed in this work and may differ for other pulse configurations.

In Fig. 2, the concentration of ions is relatively high in the center of the plasma and close to the outer edge throughout the simulation for all delay times, but the spatial–temporal distribution is affected by the separation time of the two laser pulses. The first laser pulse creates an initial plasma with low electron temperature. After a certain delay time, the main laser pulse with high intensity and the ultra-short pulse irradiate the initial plasma. The plasma expansion during the delay results in lower electron density and mass density, which facilitates more efficient energy absorption from the main pulse. This leads to a sharp rise in electron temperature and average charge state, so more highly charged ions are produced. It is clear that, when the delay time between laser pulses increases, the fraction of higher ions decreases.

In Fig. 2a–d, at a short delay time of 1.5 ns, the pre-plasma is still relatively dense, the maximum electron temperature ($T_{e\,\max}$) reaches 1584 eV, and the maximum value of average charge ($Z_{ave\,\max}$) reaches 34.4. The ion distribution in space and time reveals two main regions of Au^{20+} concentration. The first appears near the plasma's outer edge (longitudinal direction) shortly after pre-pulse irradiation, indicating that low-charge ions can be formed directly by the pre-pulse due to sufficient density for collisional ionization. The second region emerges at the plasma center following the main pulse, where enhanced electron heating increases both $T_{e\,\max}$ and $Z_{ave\,\max}$, allowing further ionization of existing ions and the formation of new ones. The presence of two ion concentration regions can be attributed to density gradients within the plasma. The plasma edge corresponds to regions of lower density and lower electron temperature. In contrast, the central region remains denser and hotter, supporting the formation of higher charge states.

In Fig. 2e–h, at a delay time of 5.8 ns, $T_{e\ \max}$ is 1356 eV, and $Z_{ave\,\max}$ is 28. The pre-plasma has expanded sufficiently, while the density remains high enough to sustain ion collisions — a condition that can be interpreted as a balance between the penetration depth of the main pulse and the thickness of the expanded plasma, enabling resonant absorption. Consequently, highly charged ions such as Au^{30+} are generated near the plasma center, with a peak ion fraction of 0.14. In contrast, the ion fraction of low-charge-state ions, like Au^{20+}, decreases and shifts toward the outer edge.

In Fig. 2i–l, when the delay time is 7.5 ns, the pre-plasma becomes more diffuse due to continued expansion, leading to a substantial reduction in both electron and mass densities. This extended expansion weakens collisional energy absorption from the main pulse. As a result, electron heating becomes less efficient, and the maximum electron temperature decreases to 1060 eV. However, the average charge state remains at 28. This stability is primarily attributed to localized hot electron generation near the plasma center via non-collisional laser absorption mechanisms. The ion spatial–temporal distribution shows a similar structure to that observed at 5.8 ns (see Fig. 1e–h), but with a slight decrease in the ion fraction.

In Fig. 2m–p, at a long delay time of 9.8 ns, the pre-plasma is highly expanded, significantly reducing the energy coupling of the main pulse. As a result, $Z_{ave\,\max}$ drops to 23 — the lowest among all cases — signaling insufficient electron heating. The plasma undergoes inward retraction due to the pressure gradient caused by the main laser pulse, compressing the low-density plasma and modifying its spatial structure. A sharp decline in the Au^{30+} ion fraction is observed (down to 4.5×10^{-3}), while Au^{20+} reaches its maximum (0.70), particularly near the outer plasma edge. The presence of two distinct concentration regions is even more evident in this case. The first region (outer edge) becomes dominant, while the second region (center) weakens progressively for higher charge states, reflecting insufficient electron temperature and density to sustain further ionization.

Figure 3 illustrates the time evolution of the maximum gold ion fraction for ion stages Au^{19+}–Au^{34+} at a certain cell of the simulation mesh for different separation times. As illustrated in Fig. 3a–d, the ion fraction of Au^{19+}–Au^{28+} will be increased within the first laser pulse of 10 ns and then begin to reduce slightly after that. Thereafter, the ion fraction increases rapidly to its maximum value, attributed to the high intensity of the second laser pulse. Additionally, Fig. 3a–c shows that the appearance of high-charge ions larger than Au^{28+} occurs with the onset of the main pulse, except for Fig. 3d, where no high-charge ions are observed. It confirms that the low electron density at a long delay time of 9.8 ns renders the main pulse incapable of inducing higher ion charges.

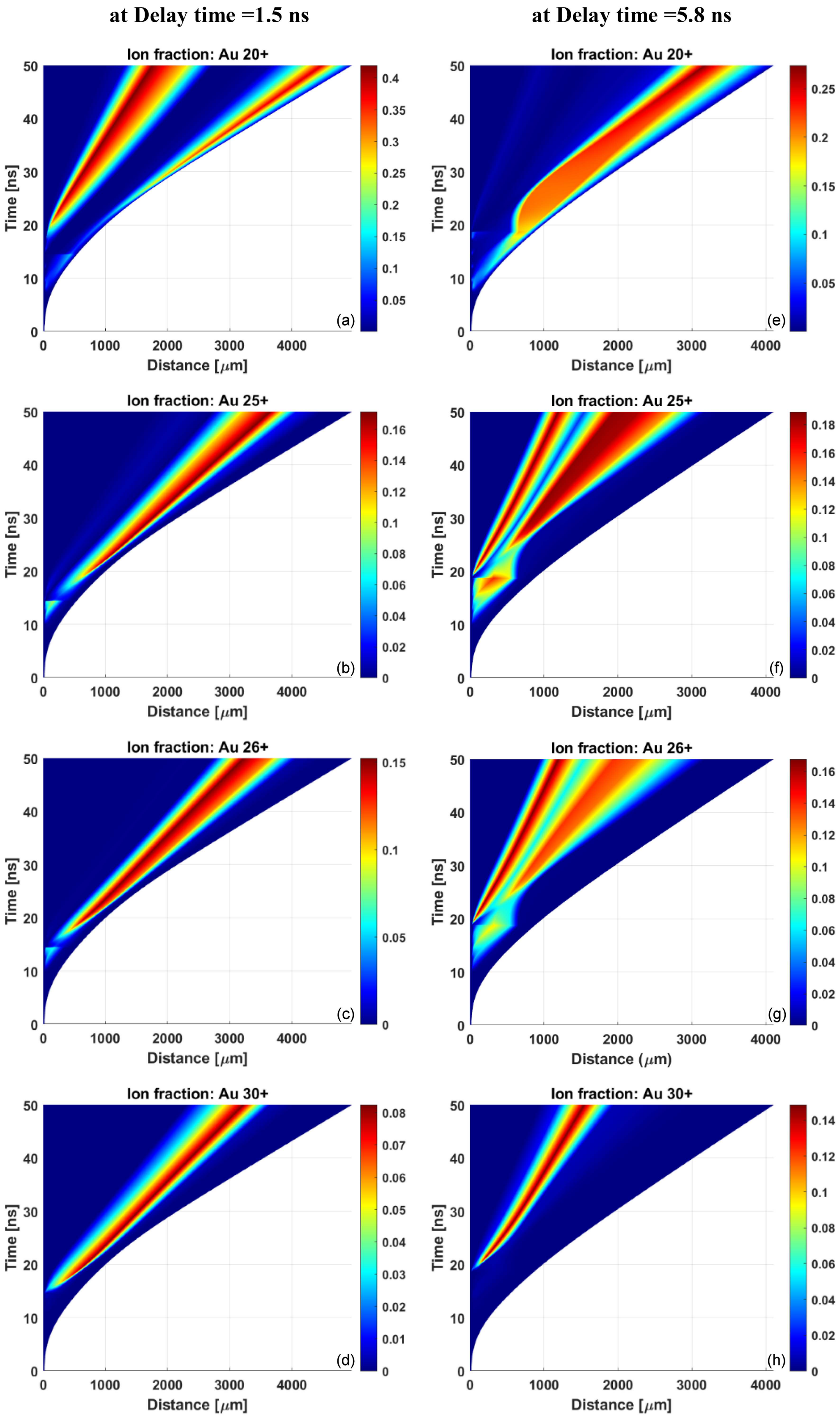

Fig. 2. Spatial–temporal maps of four ion fractions (Au^{20+}, Au^{25+}, Au^{26+}, and Au^{30+}) of a gold target that was irradiated with two pulses with delay times: (a–d) 1.5 ns, (e–h) 5.8 ns, (i–l) 7.5 ns, and (m–p) 9.8 ns.

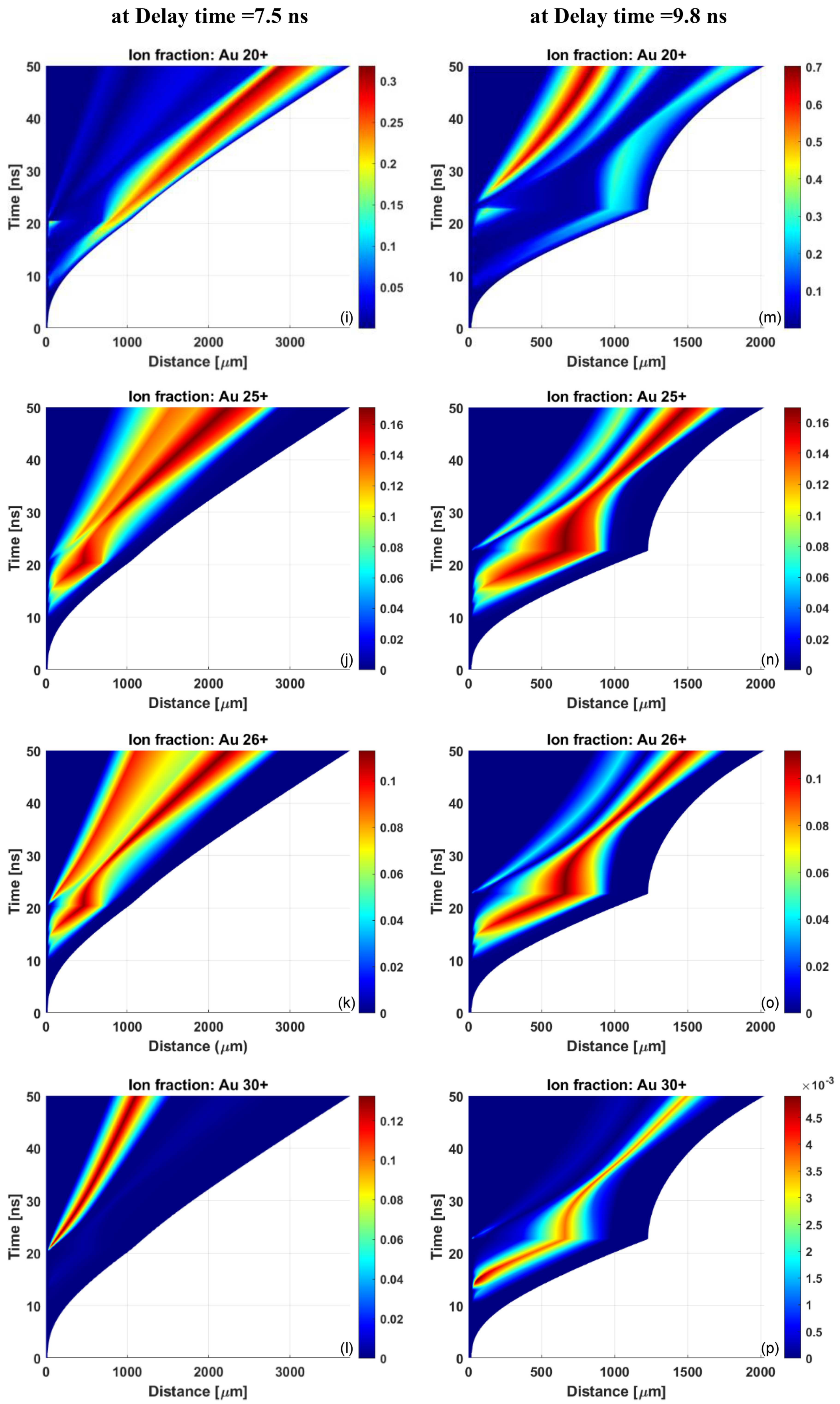

Fig. 2. Continued.

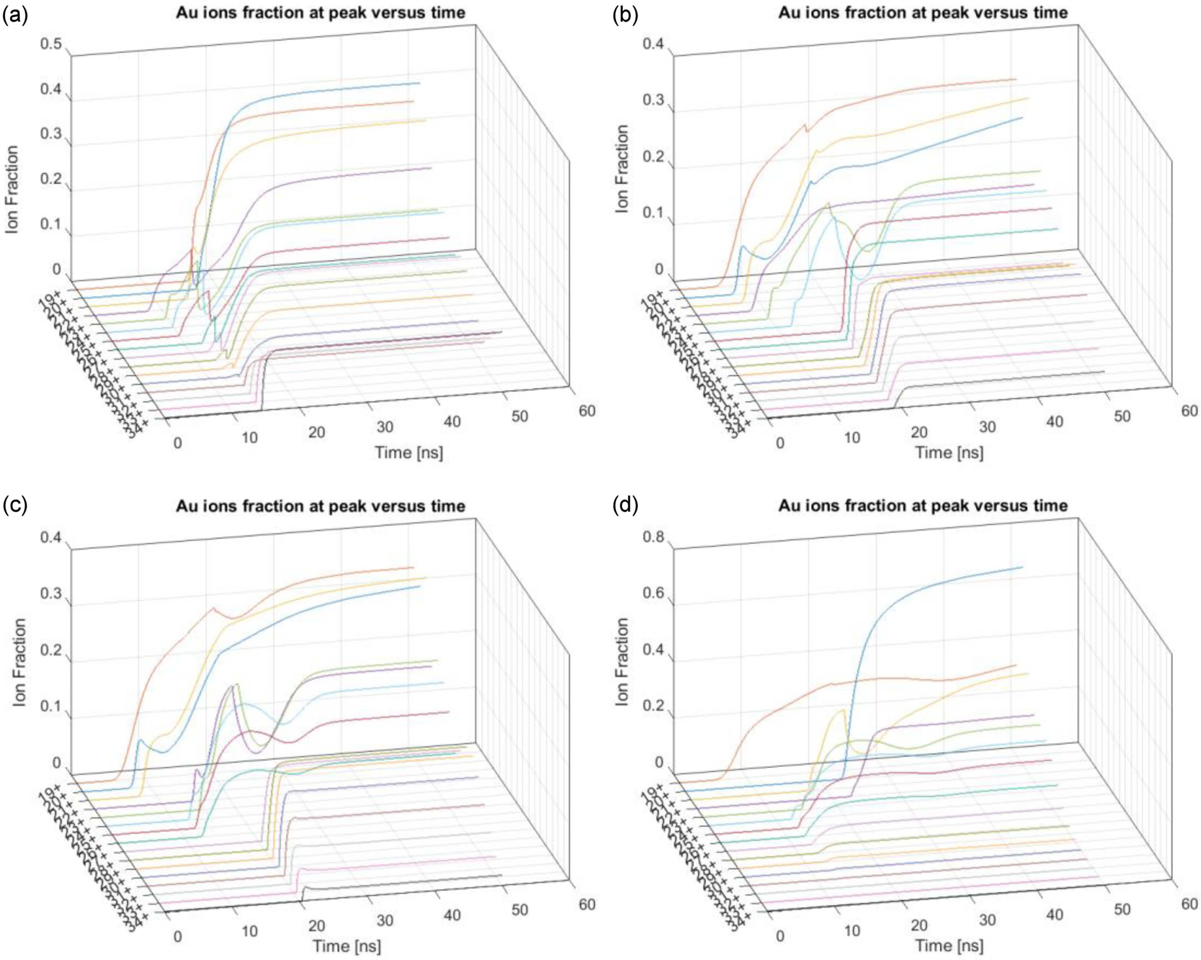

Fig. 3. The time evolution of the maximum ion fraction for Au^{19+}–Au^{34+} ions of gold plasma generated by a prepulse laser of 10 ns with a 100 fs main pulse laser at delay times: (a) 1.5 ns, (b) 5.8 ns, (c) 7.5 ns, and (d) 9.8 ns.

Table I summarizes the relationship between pulse delay, electron temperature, average charge, and the dominant ion species. At longer delay times, Au^{20+} becomes dominant due to reduced ionization, whereas at short delays (1.5 ns), multiple ion charge states appear with acceptable ion fraction, indicating that the plasma remains insufficiently expanded. During delay times of 5.8 and 7.5 ns, Au^{22+}–Au^{26+} predominate. It is evident that delay times between 5.8 and 7.5 ns provide optimal plasma conditions for the production of mid- to high-charge ions (Au^{25+}–Au^{30+}), which are key contributors to unresolved transition arrays (UTAs) for the WW region. These results are consistent with the experimental observations reported in [13] and the spectroscopic analysis in [26], where ion stages ranging from Au^{19+} to Au^{32+} were identified as key contributors to the $4f$–$5g$ transitions responsible in the WW region. The data in Table I are derived from simulation results (see Fig. 1 and Fig. 3); the "maximum ion fraction" represents the highest value of the ion fraction for each charge state during the entire simulation time, evaluated at the spatial cell where this maximum occurs. The parameter $Z_{ave\,\mathrm{max}}$ denotes the maximum value of the average charge (Z_{ave}) obtained over simulation time. Hence, the listed values correspond to the most abundant ion stages achieved during the total simulation time rather than spatial averages.

4. Conclusions

Our theoretical study elucidates the hydrodynamics of a gold plasma under a double-pulse irradiation scheme, where both the 10 ns pre-pulse and 100 fs main pulse originate from an 800 nm Ti:sapphire laser. We determined an optimum delay time between 5.8 and 7.5 ns, where the plasma scale length allows efficient resonant absorption of the main pulse, providing favorable conditions for mid- to high-ion stages (Au^{25+}–Au^{30+}) to achieve their maximum ion fractions, which are known to contribute significantly to UTAs within the water window spectral range. Notably, the highest charge states (Au^{28+} and above) emerge only after the arrival of the femtosecond main pulse, indicating the contribution of photoabsorption and inverse bremsstrahlung. At short delay time (1.5 ns), the plasma remains too dense, enhancing collisional losses and predominating lower charge states (Au^{19+}–Au^{22+}), while at long delay times (9.8 ns), excessive plasma expansion reduces energy coupling, leading to the dominance of Au^{20+} and a sharp decline in high-charge states.

Acknowledgments

The authors are thankful to the spectroscopy group at UCD for giving us the MED103 code and permission to use it, and they would also like to thank the Ministry of Higher Education and Scientific Research, Iraq, and the Department of Physics, College of Education for Women, University of Kufa, for their support.

References

[1] I. Mantouvalou, K. Witte, D. Grötzsch, M. Neitzel, S. Günther, J. Baumann, R. Jung, H. Stiel, B. Kanngießer, W. Sandner, *Rev. Sci. Instrum.* **86**, 035116 (2015).

[2] A. Bartnik, H. Fiedorowicz, P. Wachulak, T. Fok, Ł. Węgrzyński, in: *21st Czech-Polish-Slovak Optical Conference on Wave and Quantum Aspects of Contemporary Optics*, Ed. P. Zemánek, SPIE, 2018, p. 109760K.

[3] T. Tamura, G. Arai, Y. Kondo, H. Hara, T. Hatano, T. Ejima, W. Jiang, C. Suzuki, G. O'Sullivan, T. Higashiguchi, *Opt. Lett.* **43**, 2042 (2018).

[4] J. Wang, M. Kishimoto, T. Johzaki, K. Mizushima, C. Kumeda, T. Higashiguchi, A. Sunahara, H. Ohiro, K. Yamasaki, S. Namba, *Atoms* **10**, 150 (2022).

[5] C. Jacobsen, *Trends Cell Biol.* **9**, 44 (1999).

[6] M. Ayele, P.W. Wachulak, J. Czwartos, D. Adjei, A. Bartnik, M. Szczurek, L. Pina, H. Fiedorowicz, *Nucl. Instrum. Methods Phys. Res. B* **411**, 35 (2017).

[7] J. Reinhard, S. Kaleta, J.J. Abel, F. Wiesner, M. Wünsche, E. Seemann, M. Westermann, T. Weber, J. Nathanael, A. Iliou, *Microsc. Microanal.* **29**, 2014 (2023).

[8] M. Kado, M. Kishimoto, S. Tamotsu, K. Yasuda, M. Aoyama, S. Tone, K. Shinohara, *AIP Conf. Proc.* **1696**, 020019 (2016).

[9] T. Fok, P. Wachulak, K.A. Janulewicz, M. Duda, L. Wegrzynski, A. Bartnik, R. Jarocki, H. Fiedorowicz, *Acta Phys. Pol. A* **137**, 51 (2020).

[10] L. Schaper, S. Ackermann, E. Allaria et al., *Appl. Sci.* **11**, 9729 (2021).

[11] P.W. Wachulak, A. Bartnik, H. Fiedorowicz, P. Rudawski, R. Jarocki, J. Kostecki, M. Szczurek, *Nucl. Instrum. Methods Phys. Res. B* **268**, 1692 (2010).

[12] T. Fok, P. Wachulak, M. Wardzińska, A. Bartnik, P. Nyga, M.P. Nowak, H. Fiedorowicz, *Acta Phys. Pol. A* **145**, 89 (2024).

[13] T.-H. Dinh, Y. Suzuki, G. Arai, *Appl. Phys. Lett.* **107**, 121101 (2015).

[14] L. Zhang, Y. Ding, Z. Lin et al., *Nucl. Fusion* **56**, 036006 (2016).

[15] C. Kaur, S. Chaurasia, N.G. Borisenko, A. Gromov, A.A. Akunets, G.V. Sklizkov, G.A. Vergunova, S. Gus'kov, *Plasma Phys. Control. Fusion* **61**, 084001 (2019).

[16] M. Fraenkel, Y. Ehrlich, D. Rubin, Y. Ferber, G. Sturm, *Rev. Sci. Instrum.* **93**, 073509 (2022).

[17] J. Davis, Y. Frank, E. Raicher, M. Fraenkel, P. Keiter, S. Klein, R. Drake, D. Shvarts, *Rev. Sci. Instrum.* **87**, 11D609 (2016).

[18] Y. Yuan, Y. Ma, in: *Fourth Int. Symp. on High Power Laser Science and Engineering (HPLSE 2021)*, SPIE, 2021, p. 1184907.

[19] R. Fazeli, *Phys. Lett. A* **381**, 467 (2017).

[20] W.-H. Hsu, F.C.P. Masim, A. Balčytis, H.-H. Huang, T. Yonezawa, A.A. Kuchmizhak, S. Juodkazis, K. Hatanaka, *Beilstein J. Nanotechnol.* **9**, 2609 (2018).

[21] J. Christiansen, D. Ashby, K. Roberts, *Comput. Phys. Commun.* **7**, 271 (1974).

[22] A. Djaoui, "A user guide for the laser-plasma simulation code: MED103", report no. RAL-TR-96-099, 1996.

[23] L. Xin, L. Ying-Jun, Z. Jie, *Chinese Phys. Lett.* **18**, 1353 (2001).

[24] A. Cummings, G. O'Sullivan, P. Dunne, E. Sokell, N. Murphy, J. White, *J. Phys. D Appl. Phys.* **38**, 604 (2005).

[25] G. Ghani-Moghadam, S. Rezaei, M.J. Jafari, A.H. Farahbod, *Contrib. Plasma Phys.* **61**, e202100042 (2021).

[26] C. John, M. Kishimoto, Y. Matsumoto, T. Morishita, T. Higashiguchi, T. Endo, A. Sunahara, T. Johzaki, S. Namba, *High Energy Density Phys.* **37**, 100845 (2020).